



The Effect of Ar and N₂ Shielding Gas on Laser Weld Porosity in Steel, Stainless Steels, and Nickel

The reactivity and solubility of N₂ with alloying elements is believed to reduce the amount of porosity in keyhole welds, especially in 304L stainless steel

BY J. W. ELMER, J. VAJA, H. D. CARLTON, AND R. PONG

ABSTRACT

Complete, or near complete, elimination of porosity in 304L stainless steel keyhole laser welds was observed when using N₂ instead of Ar shielding gas. Partial penetration autogeneous welds were made at intermediate power levels of 2–4 kW using a continuous-wave (CW) fiber laser at travel speeds of 8–11 mm/s where porosity often occurs when using inert shielding gas. To investigate this effect further, laser welds were made in N₂ and Ar gas on three additional metals, A36 steel, 21-6-9 stainless steel, and pure nickel, that have varying properties and degrees of reactivity and solubilities with the shielding gases. Optical metallography, X-ray radiography, and X-ray computed tomography were used to characterize the porosity levels in the welds. Results show that high levels of porosity occurred in nickel, regardless of shielding gas type, while low levels or no porosity was observed in 21-6-9 for either shielding gas. However, A36 and 304L exhibited porosity in all of the welds made with Ar, and very low or no porosity when made with N₂. Computed tomography was used to quantify the porosity in selected welds, showing that the pore sizes are distributed in a monotonically decreasing trend that can be described by a two-parameter Weibull relationship ($b = 0.5429$, $a = 0.0366$). Based on the results, it is believed that the reactivity of N₂ with alloying elements, and/or its solubility in the liquid weld pool, play a significant role in reducing the amount of retained porosity in unstable keyhole welds as they solidify and cool to room temperature.

KEYWORDS

- Laser Welding • Porosity • Shielding Gas • Nitrogen • Argon • Stainless Steel
- Steel • Nickel • Computed Tomography • Weibull Relationship • Keyhole Instability

Introduction

High-brightness, continuous-wave laser welds have become attractive alternatives to high-power-density electron beam welds due to their ability to operate in atmospheric conditions, whereas nearly all electron beam welds are performed in high vacuum (Ref. 1). The economic advantages for atmospheric welding are many, but it can introduce potential oxygen contamina-

tion to the weld and can lead to undesired levels of porosity, spatter, and slag. To protect laser welds from oxygen contamination, He and Ar inert gases are often used (Ref. 2), where argon is often the preferred choice based on its lower cost. Reactive gases, such as N₂ and CO₂, or partial mixtures of these with inert gases, are occasionally used for laser welding when adverse metallurgical effects of these gases are not considered to be detrimental to

the metallurgy of the weld (Ref. 2). Pure N₂ shielding gas has recently been explored as a cost-effective alternative to Ar for welding steels, stainless steel, and nickel-based alloys (Refs. 3–5). These studies are motivated by different purposes, but one important observation that can be made is that porosity in deep penetrating keyhole-type welds, particularly in stainless steel alloys, is reduced when using N₂ shielding gas as compared to inert gases such as Ar or He.

The reasons for reduced porosity in nitrogen-shielded laser welds are not clear. One group shows that nitrogen helps to stabilize the keyhole using real time in-situ radiography in stainless steel (Ref. 5), but the mechanism is not known and additional studies will be required in order to determine the reasons for porosity reduction. However, it is clear that laser weld porosity formation is a complex process, involving the dynamics of the laser material interaction through a vapor-sustained keyhole, laser beam interaction with the plume, and varying material properties such as thermal diffusivity, liquid viscosity and density, gas solubility, vapor pressure, and alloy thermochemistry (Refs. 6–9).

In this investigation, a series of laser welding experiments was performed to evaluate the influence of Ar and N₂ on porosity formation in high-power, continuous-wave Yb-fiber laser welds. Different metals and alloys were welded that had varying degrees

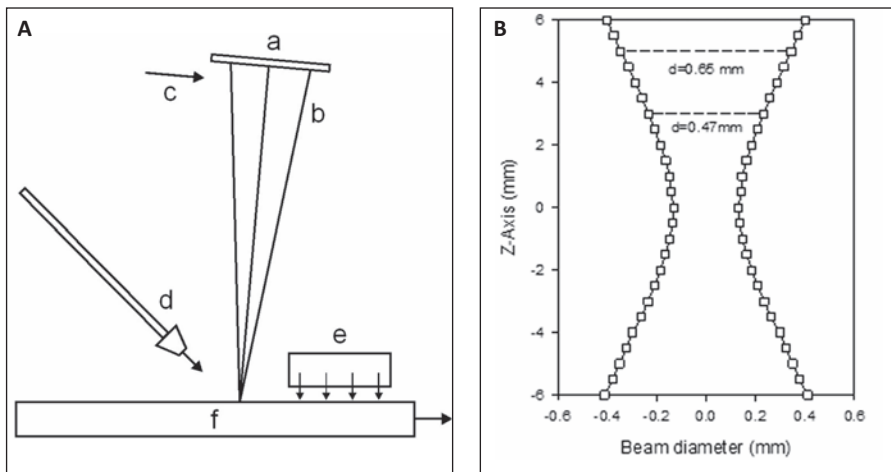


Fig. 1 — The left side schematic shows the laser weld configuration. A — Cover slide; B — laser beam with a 5-deg forward tilt; C — gas knife; D — plasma suppression gas nozzle; E — trailing gas shield; F — sample being welded, which is moving to the right under the stationary laser beam. The right side shows the beam caustic, the location of the two different plate surface positions, and their corresponding beam diameters, *d*.

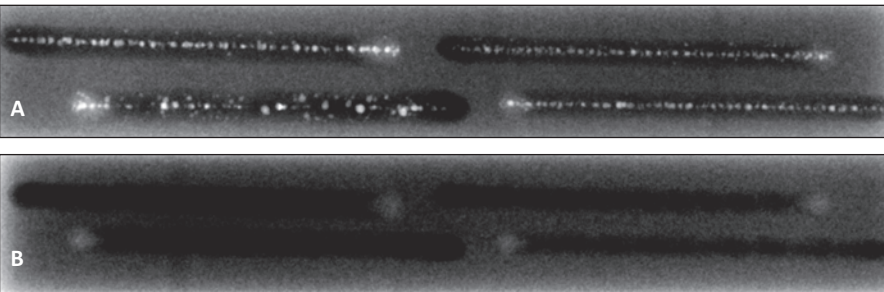


Fig. 2 — Radiographs of four preliminary laser welds made in 304L stainless steel coupons (6 ¥ 1 ¥ 0.38 in.) with (A) Ar and (B) N₂ shielding gas. Porosity (white dots) is prevalent in the welds made in Ar, but absent in the welds made with N₂.

of solubility of N₂ in the liquid weld pool, and different compositions in terms of the major alloying elements (Fe, Ni, Cr, Mn) in an attempt to isolate the effects of shielding gas and alloy composition on laser-weld-induced porosity. The resulting welds were characterized using optical metallography and quantitative X-ray radiography. The results indicate that the base metal alloy chemistry does play a large role in the formation and elimination

of porosity from the liquid melt, and that N₂ shielding gas should be considered for stainless steels and plain carbon steels, and perhaps other alloys that experience porosity in laser welds when made using inert shielding gas.

Experimental Procedures

Laser welding was performed using a 6-kW IPG Yb-fiber laser operating at 1.070±0.010 mm wavelength and de-

livered through a 200-mm fiber to the laser welding workstation. The delivery optics consist of water-cooled reflective parabolic mirrors with a 200-mm collimator and a 250-mm focusing lens. A cover slide with an antireflective coating and a laminar flow gas knife were used to protect the final focusing mirror. The laser power was measured after the beam exited the optics using a water-cooled Primes power monitor with 8-kW capacity, while the beam spot size was measured using a Primes focus monitor (model FM 120 SN1202), fitted with an 18 × 22 mm pinhole with a sensitivity of 1200 cts/(MW/cm²). The pinhole was rotated at 1875 rpm and helium gas was used to keep it from overheating. The resulting analysis measured the beam divergence, beam quality, and the beam diameter based on a second moment calculation. For the power levels used in this study, the beam had a beam parameter product BPP = 8.52 mm-mrad, M² = 2.53, Rayleigh length = 2.08 mm, and full divergence angle of 128 mrad. At sharp focus, the minimum beam diameter was measured to be 0.266 mm.

A schematic of the welding setup is shown in Fig. 1 for the stationary laser beam that is tilted 5 deg toward the front of the weld pool. A plasma suppression gas nozzle with a 3-mm-diameter orifice is directed at the beam impingement point at a 45-deg angle at 45 ft³/h (21.2 L/min) flow rate, and a trailing gas diffuser at 50 ft³/h (23 L/min) flow rate is used to minimize oxidation of the weld as it cools. The gases used were bottled high-purity Ar or bottled high-purity N₂, for the plasma suppression, gas knife, and trailing gas shield. Table 1 summarizes the laser weld and beam parameters for welds made at two different travel speeds of 8.33 and 11.5 mm/s. The beam was underfocused into the plate as illustrated in Fig. 1,

Table 1 — Summary of Weld and Beam Characteristics

Weld ID	Beam Power (W)	Weld Speed (mm/s)	Energy per Length (J/mm)	Beam Focus (mm)	Beam Diameter (mm)	Peak Power Density (kW/mm ²)	Average Power Density (kW/mm ²)	Interaction Time (d/V) (ms)
1	2300	8.33	280	-3.0	0.47	24.2	13.2	56.4
2	3200	11.5	280	-4.5	0.65	17.5	9.65	56.4
3	4200	11.5	360	-4.5	0.65	23.0	12.6	56.4
4	3000	8.33	360	-3.0	0.47	31.5	17.2	56.4

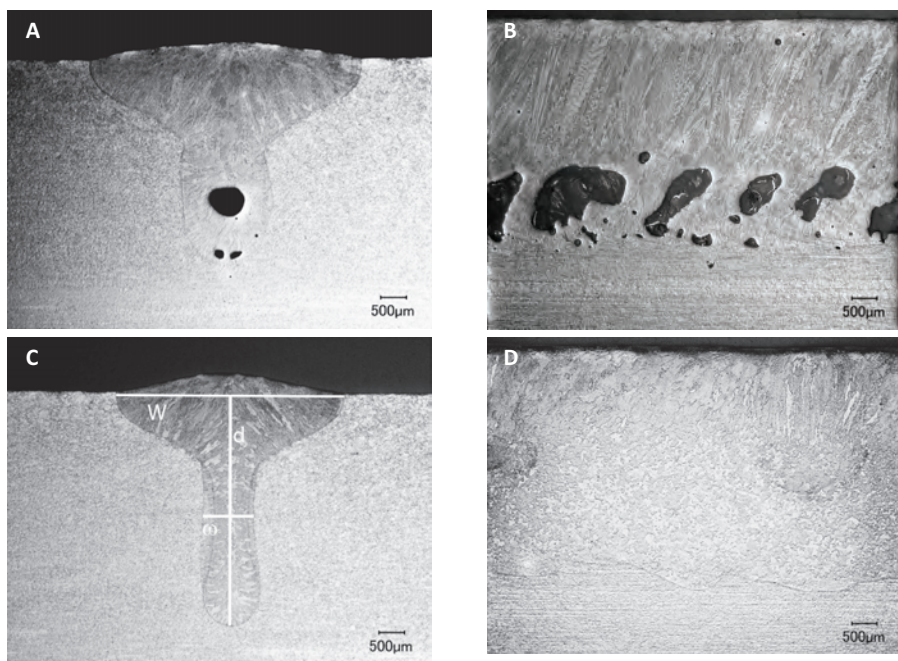


Fig. 3 — Lightly etched metallographic sections through the 2.3-kW welds made in 304L, showing porosity when using Ar gas and no porosity in N₂ gas. A — Cross section; B — longitudinal section through the weld centerline with Ar shielding gas; C — cross section; D — longitudinal section through the weld centerline with N₂ shielding gas. The plate is moving to the left in the longitudinal micrographs under a stationary laser beam. Weld dimensions are indicated in C.

which shows the measured beam caustic at two different beam diameters on the surface of the plate of $d = 0.47$ or $d = 0.65$ mm. Based on experience, the underfocused condition appears to produce slightly deeper keyhole welds than when the beam is focused at or above the surface of the plate. The combination of travel speed and beam diameters were selected so that all welds had the same interaction time (beam diameter to travel speed ratio) of 56.4 ms in an attempt to create similar keyhole interactions for the two different beam diameters.

Four different metals and alloys were chosen for the welding study, consisting of Type 304L stainless steel, 21-6-9 stainless steel (Nitronic 40), A-36 plain carbon steel, and nickel-201. The compositions of these metals are listed in Table 2, as determined using a combination of emission spectroscopy and interstitial analysis. Nitrogen contents were measured three times and the average value was reported. Note that the level of N₂ in the 21-6-9 stainless steel is 0.27 wt-%, which is midrange for Nitronic 40 specification, which has a nitrogen range of 0.15–0.40 wt-%. A total of 32 partial-penetration laser keyhole welds (4 weld parameters, 2 shielding gases, and 4 materials) were produced, and were characterized using photography, radiography, and optical microscopy. Weld coupons measuring 125–150 mm long, 25 mm wide, and 9.5 mm thick were removed from each of the materials, and two identical welds were placed on each coupon, one using Ar shielding as the shielding gas and the next using N₂ shielding gas with a 5-min purge between gas changes.

X-ray radiography was performed on the welds using conventional methods with a 450-kV Yxlon X-ray tube and a standard 5/M/10 film load. For the A-36 and Ni samples, the tube head was run at 325 kV at 2.15 mA for 3:00 and 3:15 (min:s) respectively. For the 21-6-9 and 304L, the X-ray tube head was run at 270 kV at 2.55 mA for 1:55 and 2:05 respectively. For all the radiographs, the spot size of the tube head was set at 0.4 mm, and a 2-mm Cu filter was used to improve the image quality. The films were developed, and the results were visually examined to determine qualitative levels of porosity by a Level II NDE radiographer.

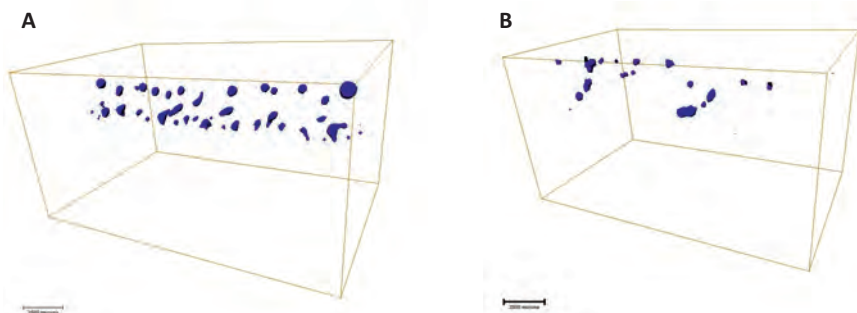


Fig. 4 — 3D CT rendering of the porosity in A36 welds made in argon shielding gas. A — A36 Weld 1 with a total porosity of 2.77 mm³; B — A36 Weld 2 with a total porosity of 0.96 mm³ in the 19-mm-long ROI.

Table 2 — Composition of the Metals and Alloys Used in This Investigation

Element	Ni-201 (wt-%)	A-36 (wt-%)	304L (wt-%)	21-6-9 (wt-%)
Fe	0.04	Bal.	Bal.	Bal.
Ni	Bal.	0.07	8.16	7.02
Cr	—	0.09	18.20	19.96
Mn	0.35	0.87	1.71	9.14
N	<0.002	0.0087	0.081	0.27
Si	0.35	0.19	0.44	0.05
P	—	0.013	0.03	0.014
S	0.01	0.002	0.0004	<0.005
O	—	—	—	<0.001
C	0.02	0.18	0.02	0.02

The nitrogen contents represent an average of three measurements, while the other elements are based on a single analysis.

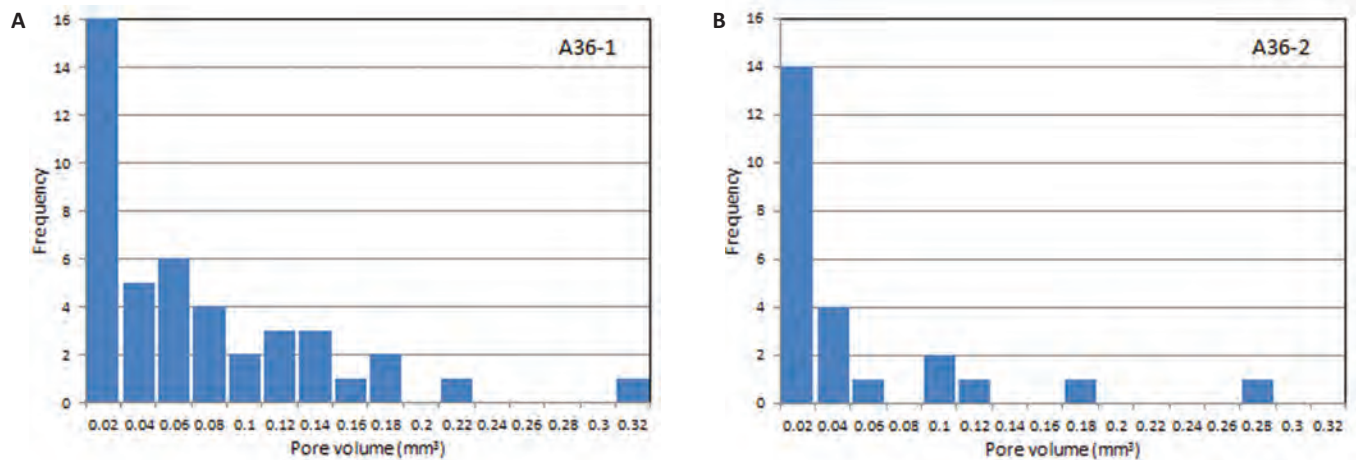


Fig. 5 — Results from the CT scan showing porosity distributions in the A36 steel Weld 1 and Weld 2 in Ar shielding gas. A36-Ar-1 was indicated to have a total pore volume of 2.77 mm³ while A36-Ar-2 was indicated to have 0.96 mm³ in the 19-mm-long ROI.

Computed X-ray tomography (CT) was further performed on some of the welds in order to quantify the amount of porosity and its location within the weld. In order to provide the highest spatial resolution, individual welds were sectioned from the original welded coupons into specimens 37 mm long, 12 mm wide and 9.2 mm thick prior to performing the CT scans. A small, flat-bottomed hole of known volume (0.8 mm diameter by 5 mm deep) was drilled in one end of the coupon to aid in volumetric quantification of porosity. These samples were placed on end, and rotated about the centerline of the weld coupon while performing CT using the same 450-kV Yxlon X-ray tube, set at 300 kV, 2.3 mA, with a spot size of 0.4 and 2 mm of Cu filtering. An Apogee CCD (AP6E) coupled to TbO₂ IQI Glass was used as the detector arrangement. A total of 480 views were taken for each sample over 360 deg of rotation. At each view, two frames were collected and these were integrated for 90 seconds each. A magnification of 1.07 was achieved, with a spatial resolution of 48 μm per pixel.

After CT data acquisition, the images were preprocessed using *IMGREC*, which is an LLNL-developed software tool. Preprocessing included converting the digital radiographs to attenuation radiographs ($\ln(I_0/I)$), removal of individual bright pixels generated from X-ray hits to the CCD camera, and filtering. The filtered images were CT reconstructed using a cone beam

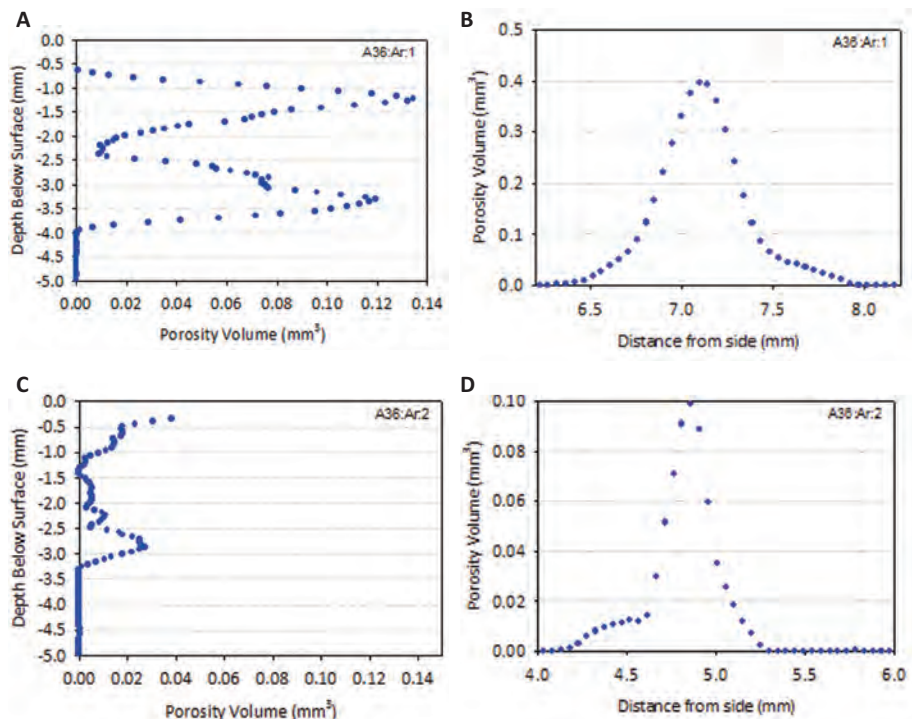


Fig. 6 — Continued results from the CT scans showing the location of the porosity in the A36 steel Weld 1 and Weld 2 in Ar shielding gas. A, B — A36-1 porosity distribution from the surface (0 mm) to the bottom (-4 mm), and from side to side of the weld, respectively. C, D — A36-2 porosity distribution from the surface (0 mm) to the bottom (-3.3 mm) of the weld, and from side to side of the weld, respectively.

algorithm to provide 3-D images of the sample and weld porosity. To analyze the porosity, segmentation of the porosity from the sample was performed using a threshold technique. To calibrate the threshold, different threshold values were used until the analysis returned a correct volume for the flat-bottomed hole. The output of the analysis is a spreadsheet that lists

all segmented porosity and their respective volumes, and the amount of porosity as a function of the distance from the front of the weld. Visualization was further performed using *Aviatio*, a commercial software package (Ref. 10).

After performing the CT scans, the welds were cross sectioned, cold mounted in epoxy, and metallographi-

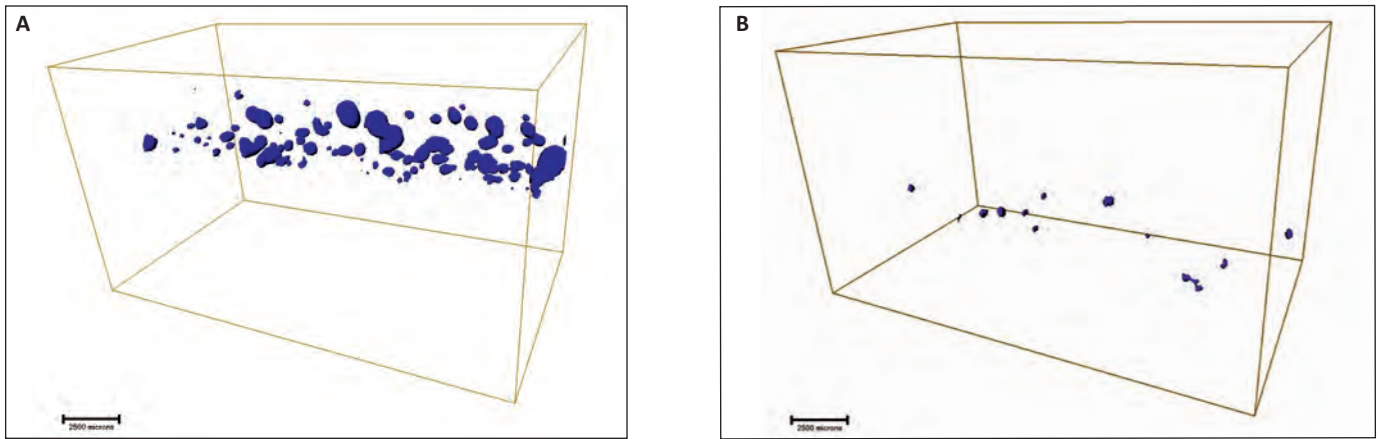


Fig. 7 — CT renderings of welds with high and low porosity made in argon shielding gas. A — 304L Weld 1 that has 7.38 mm³ of porosity; B — 21-6-9 Weld 4 that has 0.25 mm³ of porosity in the 19-mm-long ROI.

cally prepared by successive sanding on 320-, 600-, 800-, and 1200-grit paper, followed by rough polishing with 3-mm diamond paste and final polishing using a 0.1- μ m alumina suspension. After polishing, the 21-6-9 and 304L stainless steel samples were electrolytically etched in a 5% oxalic acid solution, while the A36 steel and nickel welds were chemically etched using an immersion and swabbing technique in Stead's reagent (H₂O-2.5mL, Ethanol-225mL, CuCl₂-2.5g, HCL-2.5mL, MgCl₂-10g) and Marble's reagent (CuSO₄-10g, HCL-50mL, H₂O-5mL), respectively. The etched samples were then photographed using a Keyence VHX 1000 digital microscope to observe the weld microstructure and to measure the weld pool dimensions. The weld cross-sectional area was further measured using the Keyence VHX 1000 software to calculate the area contained within a closed path perimeter line drawn around the weld fusion boundary, including the weld crown.

Results and Discussion

Porosity Formation in 304L Stainless Steel

In order to demonstrate the rather dramatic effect that nitrogen can have on reducing porosity in stainless steel welds, a series of four preliminary welds were made on 304L using Ar shielding gas on one coupon and N₂ shielding gas on the other. Two different power levels (2300 and 3000 W) and two different

beam diameters (0.47 and 0.53 mm) were used at a travel speed of 8.3 mm/s. The coupons were radiographed to film to observe porosity, and the results are shown in Fig. 2A (Ar shielding gas) and Fig. 2B (N₂ shielding gas). The radiographs were digitized and the contrast inverted so that the low density porosity appear as light regions. It is clear that all of the welds made in Ar have substantial porosity and those made in N₂ do not have any observable porosity.

Metallographic sections were made through the welds as shown in Fig. 3, which compares the 2300-W weld made with a 0.47-mm-diameter beam under Ar to those of the N₂ shielding gas. The cross section through the weld made in Ar (Fig. 3A) indicates that the porosity is localized in the bottom portion of the keyhole. Figure 3B further shows a longitudinal section through this same weld, where the pores appear to initiate at the bottom of the keyhole and grow in the same direction as the moving weld pool. The apparent periodic nature of the porosity seen in the radiographs, and the localization of the porosity to the lower portion of the keyhole, indicate that keyhole dynamics are playing a role in the porosity formation in Ar shielding gas. Metallographic cross sections of the same welds made in N₂ shielding gas are shown in Fig. 3C and D, indicating that no porosity was observed in the microstructure. It is not clear why the N₂ shielding gas is free from pores while Ar has severe porosity in 304L under identical welding conditions.

Laser weld keyhole dynamics during continuous-wave laser welding has been

studied for several decades using both experimental and modeling techniques (Refs. 5–9). These studies indicate that laser weld porosity is related to fluctuations in the keyhole depth and perturbations in its shape, which can create gas bubbles if the liquid weld pool collapses around them. These bubbles have been directly observed to circulate with the convective motion of the liquid metal, and can be trapped on the backside of the weld pool, resulting in porosity in the final weld (Refs. 5, 7). Thus, two conditions are required to create a pore in a weld. First, an unstable keyhole, or contaminant, is required to create a gas bubble in the liquid weld pool and, second, liquid convection and solidification conditions must be such that the bubble is trapped before it can escape or dissolve back into the weld pool.

One source of keyhole instability is the potential interaction of the beam with the laser plume, which can be minimized by blowing the plume out of the way by the shielding gas to minimize beam attenuation. The plume is known to be composed mainly of vaporized metal atoms and metal ions that are ejected from the keyhole, but not ionized shielding gases since they are not easily ionized at the 1-mm laser wavelength (Refs. 3, 11, 12). Higher density gases such as Ar and N₂ are more effective at removing the laser plume, and have distinct advantages over He in this respect. Table 3 summarizes some of the properties of the common shielding gases, Ar, He, and N₂, and indicates that Ar and N₂ are much closer to each other in terms of density, ionization potential, and thermal conductivity than ei-

Table 3 — Some Physical Properties of N₂, Ar, and He Shielding Gases

Property	Units	N ₂	Ar	He
Density at RT (Ref. 14)	g/liter	1.25	1.78	0.179
Density at 1600°C (Ref. 14)	g/liter	0.199	0.283	0.028
First Ionization Potential (Refs. 12, 14)	kJ/mole	1402	1520	2450
Thermal Conductivity (Refs. 14,22)	W/m-K	0.023	0.016	0.138
Threshold for Laser Breakdown (Ref.12)	GW/cm ²	82	113	—
Solubility in 21-6-9 SS (Refs. 13, 14)	wt-%	0.40	0	0
Solubility in 304L SS (Refs. 13, 14)	wt-%	0.28	0	0
Solubility in A-36 Steel (Refs. 13, 14)	wt-%	0.045	0	0
Solubility in Ni-201 (Refs. 13, 14)	wt-%	<0.0025	0	0

Solubility values are given in the liquid at 1600°C. Laser threshold for pulsed lasers at 1.064 μm wavelength and 1 atm pressure.

ther of them are to He. The size of the laser plume is largely affected by the flow rate of the gas, its density, and its thermal conductivity, since the shielding gas is not being ionized (Refs. 3, 11, 12). The higher the density of the shielding gas, the more effective it will be on blowing away the plume, and the higher its thermal conductivity, the more it will cool the plume and minimize the plume's volume. A comparison of Ar to N₂ shows that Ar is about 40% more dense than N₂, but N₂ has about 40% higher thermal conductivity, which provides a compensating effect. So, based on the physical properties of Ar and N₂ alone, it isn't clear that one gas would have a distinct advantage over the other in terms of interacting with the laser plume or stabilizing the keyhole, as long as the flow rate of the gas is sufficient to blow the laser plume out of the way.

Assuming that Ar and N₂ behave similarly in terms of beam interaction and keyhole stabilization, then differences in the amounts of porosity observed in welding 304L are likely related to the effects of these gases, or interaction of these gases, with the vapor in the keyhole or with the liquid weld pool itself. Argon, being an inert gas, does not react with the stainless steel liquid or vapor, nor does it dissolve in stainless steel liquid by a measurable amount. Therefore, removal of Ar gas bubbles from the liquid can occur only by buoyancy and the convective motion of the weld pool. Nitrogen, on the other hand, can react with Cr in metallic alloys to form chromium nitrides (Ref. 5), and can dissolve in stainless steel melts, which would reduce the amount of gas in bubbles from the liquid (Refs. 13, 14). If this dissolved N₂ does not affect the

keyhole stability, then the resulting porosity in nitrogen soluble alloys should be less than in nitrogen insoluble alloys. Since nitrogen dissolved into the stainless steel does not appear to have a strong effect on surface tension (Ref. 15), dissolved nitrogen is not expected to have a significant influence on weld convection, and probably does not affect the keyhole stability to a large extent.

Dissolution of N₂ gas bubbles into the liquid metal will depend on the solubility of nitrogen into the melt, the kinetics of the dissolution, and the amount of time the bubbles are exposed to the liquid. Assuming the kinetics are fast, then all of the N₂ gas in the entrained bubbles can be removed by a liquid melt if it has sufficient solubility of nitrogen. An estimate of the amount of gas produced by the unstable keyhole was made using the porosity produced by Ar gas shielding shown in Fig. 3 as an example. Quantitative estimates of the amount of porosity show that this weld contained approximately 6% pores by volume. Assuming an equivalent amount of porosity was initially produced by N₂ in the weld due to keyhole instability, then the increase in nitrogen content of the liquid can be calculated, assuming all of the N₂ gas bubbles formed during welding dissolve into the liquid prior to weld solidification. Using the densities shown in Table 3 for N₂ and Table 4 for 304L at 1600°C, it can be shown that 6% by volume N₂ gas bubbles, if dissolved back into the melt, will increase the nitrogen content of the liquid metal by only 0.001 wt-%. This amount of gas is well below the solubility limit of 0.280 wt-% for 304L stainless steel. Therefore, if the kinetics are fast enough, it is plausible that all of the N₂ gas bubbles created by an unstable key-

hole can be eliminated by their dissolution into the liquid melt pool, which is one possible explanation for the lack of porosity in the 304L welds made in N₂ as compared to Ar shielding gas.

The kinetics of nitrogen dissolution during arc welding of steel and stainless steel has been studied under arc welding conditions (Refs. 16, 17) and CO₂ laser welding conditions (Ref. 18). Although the kinetics for dissolution are different for arc and laser welding due to the high-temperature plasma that is created during arc welding and the corresponding dissociation of N₂ to N in the arc, there is ample evidence to suggest that nitrogen can rapidly diffuse into liquid steel melts, increasing the average nitrogen content up to, and above, saturation limits in arc welds (Ref. 17), and near saturation limits in laser welds (Ref. 18). Recent studies have shown that laser keyhole welds using a fiber laser on 304L stainless steel made in nitrogen shielding gas increased the nitrogen content of the weld metal (Ref. 19). Although the kinetics of nitrogen gas bubble dissolution are not studied here, we feel that it is highly probable that nitrogen in laser keyholes can dissolve in nitrogen soluble metals at high enough rates to be a major factor in explaining the difference in porosity observed in N₂- and Ar-shielded welds.

Relative Comparison of Porosity in 21-6-9, Nickel, A36, and 304L

In order to study the effect of nitrogen solubility on porosity formation using N₂ shielding gas, welds were made on metals and alloys that have different amounts of the major alloying elements (Fe, Ni, Cr, Mn), which have varying degrees of nitrogen solubility in the liquid metal near their melting points. Stainless steels 304L and 21Cr-6Ni-9Mn have the highest solubility of nitrogen at 0.28 to 0.40 wt-%, respectively (Refs. 13, 14). Plain carbon steel (A36) has an intermediate solubility for nitrogen similar to that of pure iron of 0.045 wt-% (Ref. 14), while nickel (Ni-201) has the lowest solubility for nitrogen of less than 0.0025 wt-% (Ref. 14). Argon is essentially insoluble in all of these metals and alloys (Ref. 14).

Laser welds were made on these alloys using several parameter sets that were designed to produce a constant beam interaction time, t' , of 56.4 ms for

Table 4 — Properties of the Metals and Alloys Used in This Investigation

Property	Units	21-6-9 SS	304L SS	A-36 Steel	Ni-201
Boiling Point Alloy (Refs. 14, 22, 25)	°C	2608	2827	2862	2918
Melting Point Alloy (Refs. 14, 22, 25)	°C	1360	1410	1538	1452
Liquid Density at MP (Ref. 14, 24)	g/cc	7.1	7.1	7.0	7.8
Liquid Viscosity at MP (Refs. 14, 22, 24)	mPa-s	—	7.0	5.1	4.2
Liquid Thermal Cond. at MP (Refs. 14, 22, 23)	W/m-K	32	29	34	65
Solid Thermal Cond. at ~1000°C/RT (Ref. 14)	W/m-K	24/12.4	29/15.9	28/59	76/88
Solid Density at ~1000°C/RT	g/cc	7.5/7.9	7.4/7.9	7.5/7.9	8.5/8.9
Solid Heat Capacity ~1000°C/RT (Ref. 14)	J/g-K	0.57/0.47	0.65/0.49	0.79/0.45	0.62/0.44
Solid Thermal Diffusivity at RT/~1000°C	(m ² /s)*10 ⁶	0.33/0.56	0.41/0.60	1.66/0.47	2.25/1.44

all of the welds. The beam interaction time is defined here as the beam diameter divided by the weld speed, and is a measure of the amount of time that a keyhole has to interact with the beam (Ref. 6). By keeping the interaction time constant, the keyhole dynamics for all of the welds should be similar. In these welds, the weld power was varied from 2300 to 4200 W, in order to produce two different levels of energy input per unit length of weld corresponding to 280 and 360 J/mm as summarized in Table 1. The average power density of these beams, defined as the beam power divided by the beam area varied from 9.65 to 17.2 kW/mm² while the measured peak power densities varied from 17.5 to 31.5 kW/mm². Bead-on-plate welds made with these parameters produced partial-penetration keyhole-type welds in all of the alloys, and all of the welds had a good surface appearance with very little spatter.

The welds were radiographed onto film and the relative amount of porosity in each weld was qualitatively evaluated by an ANSI Level II radiographer. The results are summarized in Table 5, and vary from no porosity to high levels of porosity. Comparisons of porosity levels between Ar and N₂ shielding gas for a given material, for Ar in the different materials, for N₂ in the different materials, and for different speeds and different energies per unit length of weld

reveal several interesting trends. The first two most obvious trends are that almost no porosity was observed in the 21-6-9 stainless steel welds, and that high levels of porosity were observed in all of the Ni welds, i.e., the shielding gas did not have a significant effect on porosity formation in either of these materials. However, shielding gas effects were seen in the 304L and A36 steel welds, where essentially no porosity was observed for the welds made in N₂, and various levels of porosity, from small to high amounts, were observed for the welds made in Ar.

The 21-6-9 stainless steel welds were the only welds that did not show any significant porosity in either shielding gas. Since Ar is not soluble in liquid metals, it can be concluded that 21-6-9 produced stable keyholes under all four welding conditions, i.e., these welds did not produce significant amounts of gas bubbles in the melt for either shielding gas. One possible explanation for this is that 21-6-9 contains 9 wt-% Mn, and has lower melting and boiling points, and lower enthalpy of vaporization, than the other alloys, as indicated in Table 6. These properties create higher vapor pressures at a given temperature (Refs. 9, 20), which provides higher recoil force to keep the keyhole from collapsing and creating gas bubbles and porosity (Refs. 5–9). The surface tension of the

liquid may also be affected by high Mn melts, which could also contribute to a more stable keyhole. The vapor pressure of the four major elements of the alloys studied in this investigation (Fe, Ni, Cr, Mn) is shown in Table 6 at a temperature of 1600°C (Refs. 20, 21), which is near the melting point of all of the alloys. These data indicate that there are three orders of magnitude difference in vapor pressure between $P_{Mn} > P_{Cr} > P_{Fe} > P_{Ni}$, which likely plays a significant role in keyhole stability and the formation of gas bubbles in welds.

While the 21-6-9 stainless steel welds did not show significant porosity, Ni produced high amounts of porosity in all welds and in both shielding gases. From a material standpoint, Ni has the highest boiling point of all of the major elements used in this study, has the highest difference between its melting and boiling points, and has the lowest vapor pressure at 1600°C. These conditions favor keyhole collapse and gas bubble generation in the liquid melt. Due to the very low solubility of N₂ and Ar in liquid nickel, any gas bubbles that are generated can only be removed by buoyancy and convection, and this does not appear to be taking place for the welding parameters used in this investigation. In addition, Ni has the highest thermal conductivity of the four alloys as indicated in Table 4 (Refs. 22–25). This is an additional factor that contributes to trapping the bubbles in the solidifying melt, since heat is extracted from the melt pool more quickly by the base metal, creating smaller trailing liquid pools (Ref. 8), and leaving less time for the bubbles to escape.

The A36 steel and the 304L have porosity levels between the two extremes of Ni and 21-6-9, and both were clearly affected by the type of shielding gas as qualitatively indicated by the radiography results in Table 5. With Ar shielding gas, porosity was observed in both of these alloys under all welding conditions, while essentially no porosity was observed in either alloy when N₂ shielding gas was used. Keyhole collapse and its associated porosity when using Ar shielding gas for these alloys appears similar to the effects seen in Ni, but reduced in severity in most cases. When looking at the alloy compositions, the low levels of Mn in 304L compared to 21-6-9, is the most obvious difference be-

Table 5 — Relative Amounts of Porosity in Each of the Welds Based on Initial Radiography and Qualitative Comparisons

Weld	Shielding Gas	Speed (mm/s)	Energy per Length (J/mm)	21-6-9	304L	A-36	Ni
1	Ar	8.33	280	N	H	M	H
2	Ar	11.5	280	N	M	M	H
3	Ar	11.5	360	N	M	M	H
4	Ar	8.33	360	L	M	M	H
1	N ₂	8.33	280	N	N	N	H
2	N ₂	11.5	280	N	N	N	H
3	N ₂	11.5	360	N	N	N	H
4	N ₂	8.33	360	L	L	N	H

N-none, L-low, M-medium, H-high levels of porosity.

tween these two alloys and may explain increased levels of porosity when using Ar shielding gas, since otherwise they have similar compositions. A36 also has low levels of Mn and shows increased porosity relative to 21-6-9 when welded in Ar. Cr and Ni may not be playing a large role here since 304L contains these major elements and A-36 does not, yet both alloys show similar levels of porosity when welded in Ar. Thus, if the keyhole dynamics are being affected by alloy composition, then Mn appears to be a dominant factor for the alloys studied here.

Quantitative Aspects of Porosity in 21-6-9, Nickel, A36, and 304L

Weld and Keyhole Geometry

The lack of porosity observed in A36 and 304L when using N₂ shielding gas is perhaps the most interesting observation of this study. The important question is whether or not N₂ is stabilizing the keyhole, or if the keyhole is just as unstable in N₂ as Ar but that other factors are contributing to the removal of N₂ bubbles from the melt. In an attempt to sort this out, weld cross sections were used to estimate the weld pool shape and keyhole geometry, and CT images of some of the welds were made to quantify the amount and location of porosity. The weld width, W, keyhole width, w, and weld depth, d, from the original surface were measured on the metallographic cross sections of the welds, as indicated in Fig. 3C, along with the weld pool length, L, as measured from photographs taken of the fi-

nal weld crater. These measurements, along with the weld cross-sectional areas, and weld fusion zone perimeters are summarized in Tables A1–A4 in the Appendix for all of the welds made in this investigation. Histograms of the results are further shown in the Appendix, comparing the measured weld geometries for each of the welds made in this study, based on these data.

Figure A1 compares the weld pool lengths for each of the four materials and for all of the weld parameters. It is clear that the material has a large influence on the weld pool length, where the average weld length varies by about a factor of 2× for the different materials. The trend shows increasing weld lengths from Ni to A36 to 21-6-9 to 304L, which is inversely related to their thermal diffusivities. Color coding on this figure further compares the welds made with the lower energy-per-unit length (280 J/mm) to the higher energy (360 J/mm) welds. The lower energy welds appear to be producing shorter weld pools. Figure A2 compares the keyhole and surface widths for each of the welds. The keyhole widths are consistently smaller than the surface width by a factor of about 3×. The higher energy-per-unit length welds are on average wider than the lower energy-per-unit length welds. The 21-6-9 welds had the smallest widths and the least variation of the four materials. Figure A3 compares the weld depths for each of the materials. The deepest welds were made in 21-6-9 and the shallowest were made in nickel, and the higher energy-per-unit length welds were deeper than the lower energy length welds in almost all cases. Figure A4 compares the weld cross-sectional areas. The basic trend is

similar to the weld lengths, whereby the weld cross-sectional areas are inversely related to the material's thermal diffusivity, and higher energy welds have higher cross-sectional areas.

Porosity Measurements

The initial porosity measurements were based on a qualitative evaluation of X-ray radiographs on film to determine the relative amounts of porosity in each of the welds. These data were summarized in Table 5, where the levels of porosity are labeled N for no visible pores, and L, M, H for low, medium, and high amounts of porosity, respectively. In order to quantify these levels of porosity, some of the welds were examined using computed X-ray tomography (CT), which is capable of measuring the size, distribution, and total volume of the porosity. A 19-mm region of interest (ROI) was taken along the length of weld, not including the start or stop regions, and examined by CT for at least one of each material with varying levels of porosity. Examples of the CT results are shown in Figs. 4–6 for the A36 steel Welds 1 and 2 made in argon shielding gas.

Figure 4A and B show the 3D renderings of the location of the pores in A36 Welds 1 and 2 that have 2.77 mm³ and 0.96 mm³ of porosity, respectively, in the 19-mm-long ROI. They appear to have a periodic spacing along the length of the weld, and the geometric shape of the pores and their location in the weld clearly show up in the CT images. A36-1 has the higher level of porosity in this comparison, but was still categorized as a medium level relative to some of the other welds. The largest pore that was observed in this weld had a volume of nearly 0.31 mm³, and it is clear from this image that a large number of large voids were created. The porosity appears to be more concentrated on the top and root of the weld, with less porosity at the mid keyhole location. A36-2 has less porosity, so trends in the location of the pores are not as clear, but this weld has a smaller number of pores than A36-1.

Analysis was performed on the porosity to gather statistics on the porosity size distribution, and on the location of the pores in the weld. Figure 5A, B plot histograms of the pore size

distribution for A36 Weld 1 and Weld 2, respectively. A36 Weld 1 has approximately 3× the amount of porosity by volume (2.77 mm³ vs. 0.96 mm³) and has the largest void at 0.31 mm³. Both distributions show a decreasing frequency with increasing pore size, with the largest frequencies occurring at pores less than 0.02 mm³. Further analysis of the CT data was performed on these two welds to show the distribution of porosity in the weld by integrating the total pore volume on a given slice of the ROI. Each slice measured 48 mm high, and integrations were made both from the top of the weld to the root of the weld, and from one side to the other side of the weld over the 19-mm-long ROI. These results are shown in Fig. 6A, B, for A36-1, and Fig. 6C, D for A36-2. Weld A36-1 has the greater amount of porosity, and it has a clear bimodal distribution from the top to the root of the weld, showing a high concentration of pores in both the lower keyhole region of the weld and in the top weld pool. This weld has a penetration depth of 4 mm, which can clearly be seen by the lack of porosity below this depth. The side-to-side distribution of porosity is Gaussian shaped with the highest concentration of porosity located on the weld centerline. Weld A36-2 shows a similar bimodal distribution from top to root of the weld and a weld penetration depth of 3.3 mm. However, with lower total porosity in this weld, the trends are not as clear as in the A36-1 weld.

Figure 7 shows additional 3D renderings of two welds to illustrate low and high levels of porosity for welds made in argon shielding gas. The high porosity weld is shown in Fig. 7A for 304L Weld 1 that has 7.38 mm³ of porosity. This weld had 113 voids in the 19-mm-long ROI, which is the highest number of voids observed in any of the welds. The pores are densely packed and have a distribution from small to large sizes. The largest pore in this weld was measured to be 0.91 mm³. The low-porosity weld is shown in Fig. 7B for 21-6-9 Weld 4 that has only 0.25 mm³ of porosity that is contained in a total of 15 voids in the 19-mm-long ROI, with the largest pore having a volume of 0.047 mm³. The porosity in this weld appears to be mainly concentrated at the root and the pores are of similar sizes.

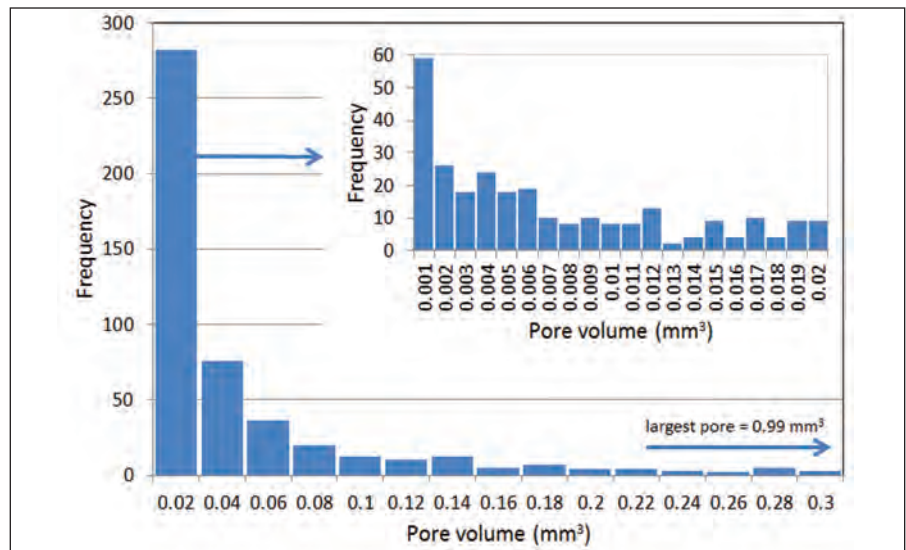


Fig. 8 — Histograms showing the porosity distribution for the 513 pores that were identified using CT methods. The inset histogram shows the distribution of the 282 smallest pores with volumes less than 0.02 mm³.

Table 6 — Physical Properties of the Major Alloying Elements Used in This Investigation

Element	Vapor Pressure at 1600°C (Refs. 20–22)	Melting point (Ref. 22)	Boiling point (Ref. 22)	Enthalpy of Vaporization (Ref. 22)
	(Torr)	(°C)	(°C)	kJ/mole
Ni	0.02	1452	3175	372
Fe	0.1	1535	2730	347
Cr	1	1615	2200	339
Mn	30	1260	2087	220

A summary of the main quantitative results from the CT runs is given in Table 7, which includes the total volumetric porosity in the 19-mm-long ROI for eleven selected welds. The highest levels of porosity were found in nickel and one of the 304L welds with porosity volumes on the order of 4–8 mm³. Medium levels of porosity found in the 304L and A36 welds were measured to be at 1–3 mm³. One 21-6-9 weld was noted to have a small amount of porosity, which measured 0.25 mm³, while the other 21-6-9 weld that had no observable porosity, as measured on the X-ray film, was determined to have a small amount of voids as detected by CT measuring 0.032 mm³.

Since the welds varied in size and shape, depending on the material and the welding parameters, the total volume of pores for each weld was normalized to the fusion zone volume for each of the 11 welds examined by CT. The fusion zone volume was calculated

by multiplying the weld cross-sectional areas (summarized in Tables A1–A4) by the 19-mm-long ROI of the CT measurements to represent the total amount of melted material in the ROI fusion zone. Table 7 reports these values as percent porosity in the weld fusion zone. The highest levels of porosity contain 3.6 to 7.4% porosity by volume. This high value of porosity is similar in magnitude to porosity generated in CW laser welds made in argon shielding gas on 304L stainless steel at about 1 m/min travel speeds by Madison et al. (Refs. 26, 27). Medium levels of porosity were characterized to contain approximately 0.5 to 2% volumetric porosity, while the low level of porosity was characterized to be less than 0.1% porosity by volume.

The CT results were further analyzed to characterize the size distribution of 513 pores that appeared in the different welds. The results show individual pore volumes varying from less than 0.001 mm³, which are present in

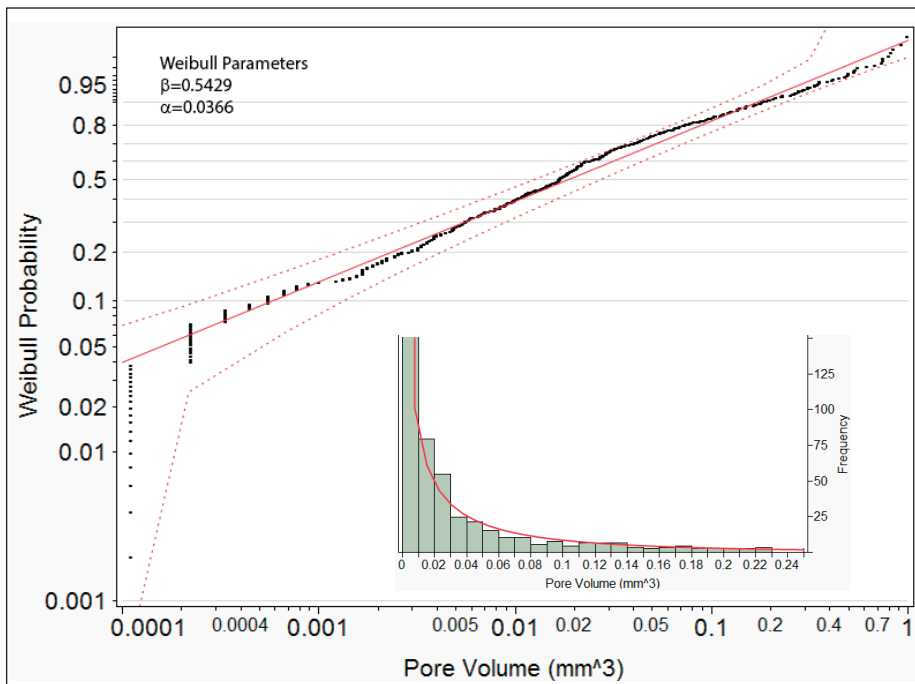


Fig. 9 — Results of the Weibull analysis of the pore size distribution, where the red solid line on the probability plot is the Weibull best fit through the 513 pores measured by CT, while the red dotted lines are the 95% confidence limits. The red curve in the inset figure is the Weibull fit to the pore distribution plotted as a histogram.

all of the welds, up to 0.99 mm³ in the highest porosity nickel weld. Figure 8 plots a histogram of the size distribution of the pores, and indicates that the largest frequency of pores occurs at the smallest volumes of less than 0.02 mm³/pore. The inset histogram further plots the distribution of the 282 smallest pores with volumes less than 0.02 mm³, indicating again that the largest frequency of pores occurs at the smallest pore volumes, now at less than 0.001 mm³/pore.

The monotonically decreasing dis-

tribution of pore size with pore volume can be described by a Weibull relationship as in Equation 1 (Ref. 28).

$$f(P) = \frac{\beta}{\alpha} \left(\frac{P}{\alpha}\right)^{(\beta-1)} \exp\left(-\left(\frac{P}{\alpha}\right)^\beta\right) \quad (1)$$

In this equation, the pore size, P, is represented as a continuous function of two parameters, β , the Weibull shape factor, and α , the Weibull scaling parameter. The complete data set of 513 pores was fit by the two-param-

eter Weibull relationship using a statistical data analysis package (Ref. 28) to determine β and α . The results of the Weibull analysis are plotted in Fig. 9, showing a good fit to the data on the probability plot with $\beta = 0.5429$ and $\alpha = 0.0366$. Data binning at low pore sizes are a result of the CT resolution having a 48 mm pixel width, which corresponds to a detected volume being displayed in increments of 0.00011 mm³. The calculated β parameter of 0.5429, being less than unity, describes the monotonically decreasing function of the frequency of pore size with increasing pore diameter, and is plotted as the red curved line on the histogram inset into Fig. 9. The very high fraction of small pores indicates that the laser welding process produces an abundance of tiny bubbles in the weld pool, and it can be speculated that some of these bubbles grow to create some of the large pores that are observed before the weld pool solidifies and traps them in place.

Summary and Future Work

Observations from this study show the beneficial results of nitrogen shielding gas on reducing porosity in laser keyhole welds made in 304L stainless steel and A36 carbon-manganese steel relative to welds made in argon. This effect may be the result of improved keyhole stability provided by nitrogen, or other factors such as the solubility and/or reactivity of nitrogen with the liquid weld pool that can remove nitrogen porosity from the weld. Welds in additional materials were made to help sort out the possible mechanisms re-

Table 7 — Summary of CT Results on Selected Welds for a 19-mm-Long Region of Interest along the Length of the Weld

Material	Weld No-Gas	Qualitative Level of Porosity (Table 5)	Number of Pores Measured by CT	Total Volumetric Porosity by CT (mm ³)	Total Melt Zone Volume (mm ³)	Porosity Per Unit Volume of Weld (%)
Ni	1-Ar	H	78	7.61	102	7.43
Ni	2-Ar	H	67	6.84	118	5.77
Ni	1-N ₂	H	82	4.18	99.8	4.19
304L	1-Ar	H	113	7.38	205	3.60
A-36	1-Ar	M	44	2.77	141	1.91
A-36	4-Ar	M	43	3.02	285	1.06
A-36	2-Ar	M	24	0.96	106	0.90
304L	2-Ar	M	36	1.39	175	0.79
A-36	3-Ar	M	9	1.49	287	0.52
21-6-9	4-Ar	L	15	0.25	272	0.09
21-6-9	3-Ar	N	2	0.032	274	0.01

A total of 513 pores were identified in the 11 welds examined by CT.

sponsible for the porosity formation. These results showed that nitrogen does not eliminate or reduce porosity from welds made in nickel, and that argon does not produce porosity in 21-6-9 stainless steel. These results are believed to be due to the keyhole stabilizing elements, such as Mn in 21-6-9, and the lack of them in Ni, combined with the solubility of nitrogen in 21-6-9 and the lack of solubility of nitrogen in Ni. All of the welds made in this investigation were made at atmospheric pressure, where the laser plume and shielding gas interactions with the beam are relatively high. Future work is planned at reduced pressure in an attempt to further reduce porosity in laser keyhole welds by promoting more stable keyholes due to lowered pressure acting on the keyhole, and by reducing entrapment of shielding gas in the keyhole.

Conclusions

Porosity formation in continuous-wave keyhole laser welds made at two beam diameters and a constant interaction time of 56.4 ms is affected by the type of shielding gas used to make the welds, and the composition of the material being welded.

The lowest levels of porosity were observed in 21-6-9 stainless steel, which displayed low or no porosity in either shielding gas. Low porosity is presumed to be the result of the formation of a stable keyhole due to the high content of Mn in this alloy that aids in keeping the keyhole open due to its high vapor pressure.

The highest levels of porosity, up to 7.5% by volume, were observed in pure nickel, which displayed high levels of porosity for both argon and nitrogen shielding gas. The low vapor pressure of nickel is believed to be related to a higher keyhole instability, and thus higher initial porosity generation. The relatively high thermal diffusivity of nickel is further responsible for trapping much of this porosity before it has a chance to be transported out of the liquid weld pool before the weld solidifies.

Mixed levels of porosity were observed in both A36 steel and 304L stainless steel, which displayed a strong correlation with shielding gas type. The range of porosity varied from medium to high levels in argon

shielding gas, and little or no porosity when these alloys were welded in nitrogen shielding gas.

Solubility and reactivity of the shielding gas with the liquid weld pool appear to be playing a large role in the retention of porosity in laser keyhole welds that produce gas bubbles during welding due to keyhole instability. High solubility and/or high reactivity of the shielding gas with the liquid in the weld pool acts to reduce or eliminate the gas bubbles, resulting in lower or no measurable porosity in nitrogen shielding gas than welds made in inert gas such as argon.

Computed X-ray tomography (CT) was used to quantify the amount of porosity in selected welds in order to analyze the distribution of pore sizes. The results, based on 513 pores, showed that the pore size distribution can be described by a two-parameter Weibull relationship with $\beta = 0.5429$, and $\alpha = 0.0366$. These parameters describe a distribution that has a monotonically decreasing frequency with increasing pore size, and can be used to predict the probability of generating pores of a given size for quality assurance purposes. This distribution suggests that the laser keyhole welding process produces many small bubbles that may coalesce to larger sizes during the time that the weld solidifies.

Acknowledgments

The authors would like to thank LLNL coworkers T. H. Gooch for assisting with laser welding and C. L. Evans and J. J. Embree for performing optical metallography of the welds, and J. A. Rodriguez, R. Thompson, W. D. Brown, and B. J. Fix of the Non Destructive Evaluation group at LLNL for radiography and CT reconstruction. This work was performed under the auspices of the U.S. Department of Energy by Lawrence Livermore National Laboratory under Contract DE-AC52-07NA27344.

References

1. Elmer, J. W., Hochanadel, P. W., Lachenberg, K., Caristan, C., and Webber, T. 2011. Introduction to High Energy Density Electron and Laser Beam Welding. *ASM Handbook of Welding*, 11th Edition, ASM International, Metals Park, Ohio, pp. 507–513.
2. *Recommended Practices for Shielding Gases for Welding and Plasma Arc Cutting*, ANSI AWS C5.10-94. 1994. American Welding Society, Miami, Fla.
3. Kuo, T-Y, and Lin, Y. D. 2007. Effects of different shielding gasses and power waveforms on penetration characteristics and porosity formation in laser welding of Inconel 690 alloy *Materials Transactions* 48(2): 219–226.
4. Shin, M., and Nakata, K. 2010. Weld bead formation by a 10 kW class high power fiber laser on 16 mm thickness carbon steel plate. *Trans. JWRI* 39(1): 33–38.
5. Kawahito, Y., Mizutani, M., and Katayama, S. 2009. High quality welding of stainless steel with 10 kW high power fiber laser. *Science and Technology of Welding and Joining* 14(4): 288–294.
6. Matsunawa, A., and Semak, V. 1997. The simulation of front keyhole wall dynamics during laser welding. *J. Phys. D: Appl. Phys.* 30: 798–809.
7. Zhao, H., Niu, W., Zhang, B., Lei, Y., Kodama, M., and Ishide, T. 2011. Modeling of keyhole dynamics and porosity formation considering the adaptive keyhole shape and three-phase coupling during deep-penetration laser welding. *J. Applied Physics D: Applied Physics* 44: 485302.
8. Rai, R., Elmer, J. W., Palmer, T. A., and DebRoy, T. 2007. Heat transfer and fluid flow during keyhole mode laser welding of tantalum, Ti-6Al-4V, 304L stainless steel and vanadium. *Journal of Physics D: Applied Physics* 40 (18): 5753–5766.
9. DebRoy, T., Basu, S., and Mundra, K. 1991. Probing laser induced metal vaporization by gas dynamics and liquid pool transport phenomena. *J. Appl. Phys.* 70(3): 1313–1319.
10. Avizo. 3D analysis software for scientific and industrial data. <http://www.vsg3d.com/avizo/overview>
11. Greses, J., Hilton, P. A., Barlow, C. Y., and Steen, W. M. 2004. Plume attenuation under high power Nd: yttrium-aluminum-garnet laser welding. *Journal of Laser Applications* 16(1): 9–15.
12. Davis, J. P., Smith, A. L., Giranda, C., and Squicciarini, M. 1991. Laser-induced plasma formation in Xe, Ar, N₂, and O₂ at the first four harmonics. *Applied Optics* 30: 4358–4364.
13. Dischino, A., Kenny, J. M., Mecozzi, M. G., and Barteri, M. 2000. Development of high nitrogen, low nickel, 18%Cr austenitic stainless steels. *J. Materials Science* 35: 43803–43808.
14. C. J. Smithells, E. A. Brandes, and G. B. Brook. 1992. *Smithells Metal Reference Book*, seventh ed., Butterworth-Heinemann Ltd., Oxford, UK.

15. Li, Z., Mukai, K., ZeZe, M., and Mills, K. C. 2005. Determination of the surface tension of liquid stainless steel. *Journal of Materials Science* 40: 2191-2195.

16. Palmer, T. A., and DeRoy, T. 2000. Numerical modeling of enhanced nitrogen dissolution during gas tungsten arc welding. *Metallurgical and Materials Transactions B*, 31B, pp. 1371-1385.

17. Du Toit, M., and Pistorius, P. C. 2003. Nitrogen control during the autogeneous arc welding of stainless steel part 2: A kinetic model for nitrogen absorption and desorption. *Welding Journal* 82(9): 231-s to 237-s.

18. Dong, W. et al. 2003. Nitrogen absorption by iron and stainless steels during CO₂ laser welding. *Metallurgical and Materials Transactions B*, 34B, pp. 75-82.

19. Unpublished research by Kevin Faraone at the National Security Campus, Kansas City, Mo., October, 2014.

20. Block-Bolten, A., and Egar, T. W. 1984. Metal vaporization from weld pools. *Metallurgical Transactions B* 15(3): 461-469.

21. Schwartz, M. M. 1987. *Brazing*. ASM International, Metals Park, Ohio.

22. Iida, T., and Guthrie, R. 1988. *The Physical Properties of Liquid Metals*, Oxford University Press.

23. Nishi, T., Shibata, H., Ohta, H., and Wasead, Y. 2003. Thermal conductivities of molten iron, cobalt, and nickel by laser flash method. *Metallurgical and Materials Transactions A*, 34A, pp. 2801-2807.

24. Kobatake, H., and Brillo, J. 2013. Density and viscosity of ternary Cr-Fe-Ni

liquid alloys. *Journal of Materials Science* 48, pp. 6818-6824.

25. Mills, K. C. 2002. *Recommended Values of Thermophysical Properties for Selected Commercial Alloys*, ASM International, Materials Park, Ohio.

26. Madison, J. D., and Aagesen, L. K. 2012. Quantitative characterization of porosity in laser welds of stainless steel. *Scripta Materialia* 67: 783-786.

27. Madison, J. D., Aagesen, L. K., Battaile, C. C., Rodelas, J. M., and Payton, T. K. C. S. 2013. Coupling 3D quantitative interrogation of weld microstructure with 3D models of mechanical response. *Metall. Microstruct. Anal.* 2: 359-363.

28. JMP. 2010. Version 9.0.0. SAS Institute, Inc., Cary, N.C.

Appendix

Summary of Weld Pool Geometries

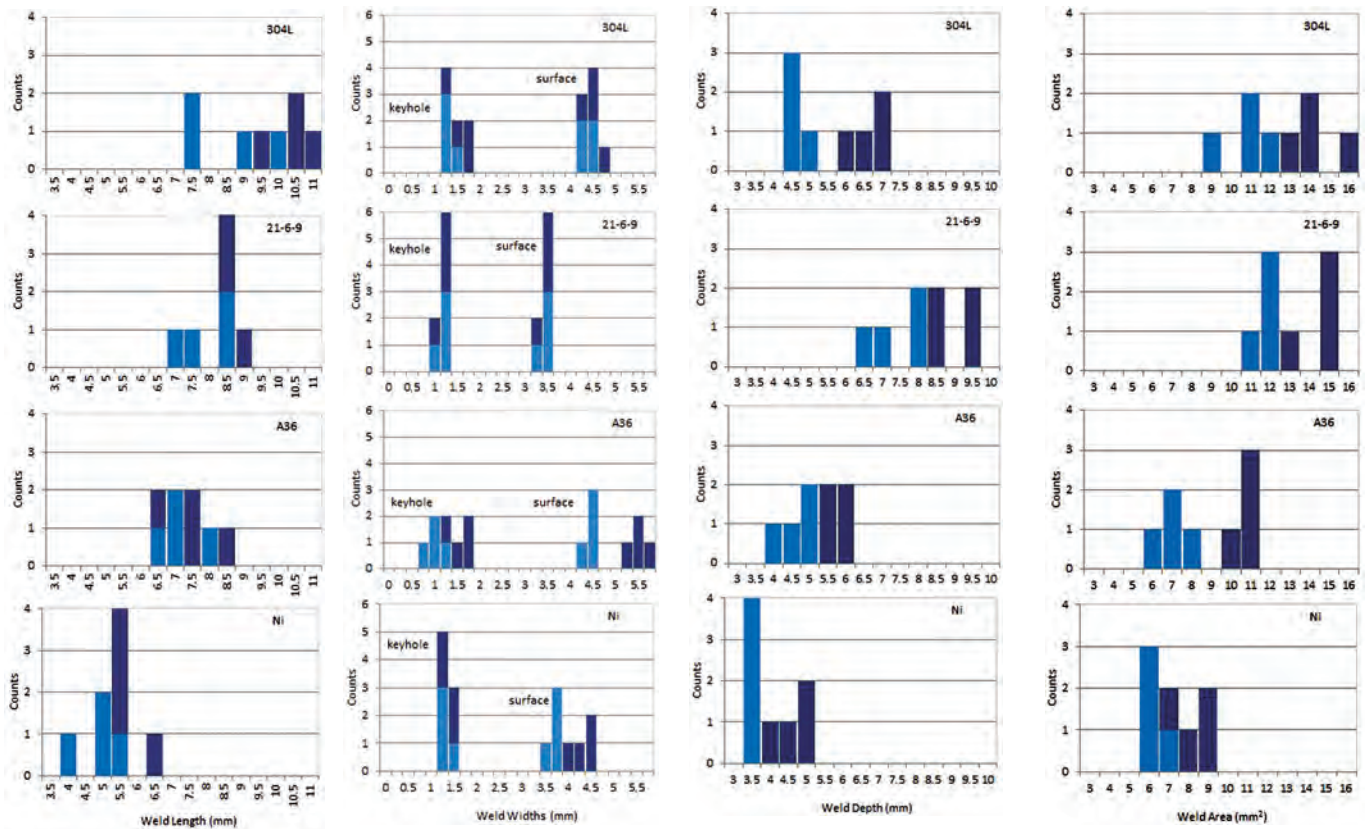


Fig. A1 — Histograms showing the distribution of the weld lengths for the 32 welds. The darker shaded regions represent the welds at 360 J/mm, while the lighter shaded regions represent the welds made at 280 J/mm.

Fig. A2 — Histograms showing the distribution of the weld widths for 32 welds. The key-hole widths, w , are plotted along with the width at the surface of the plate, W . The darker shaded regions represent the welds at 360 J/mm, while the lighter shaded regions represent the welds made at 280 J/mm.

Fig. A3 — Histograms showing the distribution of the weld depths for the 32 welds. The darker shaded regions represent the welds at 360 J/mm, while the lighter shaded regions represent the welds made at 280 J/mm.

Fig. A4 — Histograms showing the distribution of the weld cross-sectional areas for the 32 welds. The darker shaded regions represent the welds at 360 J/mm, while the lighter shaded regions represent the welds made at 280 J/mm.

Table A1 — A-36 Steel Weld Pool Geometry Measurements and Calculated Cross-sectional Areas

Weld	Shielding Gas	Weld Depth (mm)	Weld Width (mm)	Keyhole Width (mm)	Weld Area (mm ²)	Weld Perimeter (mm)	Weld Length (mm)
1	Ar	3.53	4.46	1.37	7.4	13.7	6.4
2	Ar	4.29	4.40	0.843	5.6	13.1	6.1
3	Ar	5.68	5.40	1.05	10.3	19.1	8.1
4	Ar	5.27	5.66	0.850	10.4	18.7	7.4
1	N ₂	4.65	4.06	0.735	6.5	14.5	7.8
2	N ₂	4.70	4.27	0.667	6.3	16.2	6.8
3	N ₂	5.83	5.03	0.980	10.4	18.4	7.2
4	N ₂	5.34	5.42	0.750	8.5	17.4	6.1

Table A2 — Nickel Weld Pool Geometry Measurements and Calculated Cross-sectional Areas

Weld	Shielding Gas	Weld Depth (mm)	Weld Width (mm)	Keyhole Width (mm)	Weld Area (mm ²)	Weld Perimeter (mm)	Weld Length (mm)
1	Ar	3.10	3.48	1.29	5.39	11.9	4.2
2	Ar	3.42	3.62	1.19	6.24	13.9	5.2
3	Ar	4.56	4.29	1.17	8.74	16.2	6.1
4	Ar	4.20	4.30	1.42	8.27	15.1	5.4
1	N ₂	3.03	3.59	1.14	5.25	12.3	3.9
2	N ₂	3.61	3.51	1.14	5.61	12.5	4.5
3	N ₂	4.63	4.13	1.06	8.00	16.3	5.5
4	N ₂	3.49	3.86	1.33	6.83	13.7	5.2

Table A3 — 304L SS Weld Pool Geometry Measurements and Calculated Cross-sectional Areas

Weld	Shielding Gas	Weld Depth (mm)	Weld Width (mm)	Keyhole Width (mm)	Weld Area (mm ²)	Weld Perimeter (mm)	Weld Length (mm)
1	Ar	4.78	4.01	1.39	10.8	16.5	7.1
2	Ar	4.89	4.25	1.17	9.21	17.2	8.7
3	Ar	7.17	4.72	1.50	13.3	22.5	10.6
4	Ar	6.74	4.29	1.62	15.6	20.3	10.3
1	N ₂	4.56	4.42	1.01	7.10	17.1	7.4
2	N ₂	5.10	4.38	1.03	9.09	17.6	9.7
3	N ₂	7.04	4.40	1.52	13.5	21.1	10.3
4	N ₂	6.31	4.05	1.21	13.0	19.0	9.1

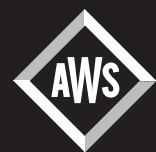
Table A4 — 21-6-9 SS Weld Pool Geometry Measurements and Calculated Cross-sectional Areas

Weld	Shielding Gas	Weld Depth (mm)	Weld Width (mm)	Keyhole Width (mm)	Weld Area (mm ²)	Weld Perimeter (mm)	Weld Length (mm)
1	Ar	8.48	3.31	1.06	11.6	22.4	8.3
2	Ar	8.48	3.20	0.98	11.7	20.3	7.1
3	Ar	9.70	3.47	0.92	14.4	25.3	8.4
4	Ar	8.91	3.36	1.11	14.3	23.7	8.4
1	N ₂	6.78	3.44	1.21	11.1	19.3	6.8
2	N ₂	8.12	3.30	1.12	10.3	20.1	8.1
3	N ₂	9.90	3.36	1.10	15.0	28.9	8.4
4	N ₂	8.2	3.05	1.15	12.9	21.6	8.7

Publish Your
Research in the

WELDING
Journal
and You'll Get

- Your research sent to more than 70,000 **American Welding Society** members
- Your published paper posted on the AWS Web site for **FREE** access worldwide (www.aws.org/w/a/research/index.html)
- The most recent Impact Factor of 1.143
- No page charges
- Your paper printed in full color
- Electronic submission and tracking through Editorial Manager (www.editorialmanager.com/wj)
- Every research paper published in the **Welding Journal** since 1970 available **FREE** on the AWS Web site (www.aws.org/wj/supplement/supplement-index.html)



American Welding Society

By far, the most people, at the least cost, will be exposed to your research when you publish in the world-respected **Welding Journal**